

Atomic Dispersion via High-Entropy Liquid Metal Alloys

Francois-Marie Allieux,* Sahar Nazari, Mohammad B. Ghasemian, Ali Zavabeti, Zengxia Pei, Josh Leverett, Somayeh Rafezadeh, Amar K. Salih, Curtis P. Irvine, Mahroo Baharfar, Laetitia Bardet, Moonika S. Widjajana, Yuan Chi, Dorna Esrafilzadeh, Ali R. Jalili, Nima Haghdadi, Jianbo Tang, Kevin J. Laws, Cuong Ton-That, Torben Daeneke, Rahman Daiyan, Md Arifur Rahim, and Kourosh Kalantar-Zadeh*

Gallium-based liquid metal alloys exhibit unconventional and intriguing properties as metallic solvents, demonstrating an exceptional potential to dissolve and reconfigure a vast array of elements within the liquid metal matrix. Leveraging on these distinctive characteristics of gallium-based alloys, the synthesis of high-entropy liquid metal alloys (HELMAs) in low dimensions is reported. The nanoscale HELMAs offer advantages including the solvation of multiple metallic elements at room temperature, while promoting their atomic dispersion at elevated concentrations. Entropy estimations for HELMAs surpass those of high-temperature molten metals, leading to the realization of high-entropy liquid metal systems at room temperature. Through a proof-of-concept hydrogen evolution reaction comparison, the potential of these HELMAs in enhancing the activities of nanocatalysts is demonstrated. In this case, atomic dispersion of Pt is shown in senary Galn-AuCuPtPd HELMA, contrasting with lower entropy systems in which Pt forms discernible clusters. These presented features can lead to catalytic systems with enhanced and tailored activities.

1. Introduction


Liquid metals exhibiting fluidic characteristics at or near ambient conditions are increasingly capturing attention in materials science.^[1] Their distinct physicochemical properties, coupled with their broad utility as metallic solvents, are fueling a surge of innovation and new possibilities in a vast range of scientific domains.^[2,3] A significant portion of the field of liquid metals started to focus on liquid metal-supported catalysts, where one constituent is incorporated in the liquid metal support acting as a free-flowing catalytic element within the metallic matrix at the single atomic level or as clusters.^[4–6] Such configurations allow accessing the near room temperature catalytic performance of high

F.-M. Allieux, M. B. Ghasemian, Z. Pei, M. S. Widjajana, M. A. Rahim, K. Kalantar-Zadeh
School of Chemical and Biomolecular Engineering
The University of Sydney
Sydney, NSW 2008, Australia
E-mail: f.allieux@sydney.edu.au; kourosh.kalantarzadeh@sydney.edu.au

F.-M. Allieux, S. Nazari, M. B. Ghasemian, J. Leverett, M. Baharfar, L. Bardet, M. S. Widjajana, Y. Chi, A. R. Jalili, J. Tang, R. Daiyan, M. A. Rahim, K. Kalantar-Zadeh
School of Chemical Engineering
University of New South Wales (UNSW)
Sydney, NSW 2052, Australia

A. Zavabeti
Department of Chemical Engineering
The University of Melbourne
Parkville, VIC 3010, Australia

A. Zavabeti, T. Daeneke
School of Science
RMIT University
Melbourne, VIC 3001, Australia

 The ORCID identification number(s) for the author(s) of this article can be found under <https://doi.org/10.1002/ssstr.202400294>.

© 2024 The Author(s). Small Structures published by Wiley-VCH GmbH. This is an open access article under the terms of the Creative Commons Attribution License, which permits use, distribution and reproduction in any medium, provided the original work is properly cited.

DOI: 10.1002/ssstr.202400294

S. Rafezadeh, A. K. Salih, C. P. Irvine, C. Ton-That
School of Mathematical and Physical Sciences
University of Technology Sydney
Ultimo, NSW 2007, Australia

D. Esrafilzadeh
Graduate School of Biomedical Engineering
UNSW
Sydney, NSW 2052, Australia

N. Haghdadi, K. J. Laws
School of Materials Science & Engineering
UNSW Sydney
Kensington, NSW 2052, Australia

N. Haghdadi
Department of Materials
Imperial College London
London SW7 2AZ, UK

T. Daeneke
School of Engineering
RMIT University
124 La Trobe Street, Melbourne 3000, Australia

R. Daiyan
School of Minerals and Energy Engineering
The University of New South Wales
Sydney 2052, Australia

melting point metals in a pseudo liquid state, in minute quantities.^[4] Until now, liquid metal alloys and liquid metal-supported catalysts have been limited to include only a few elements and have not yet reached the realm of high-entropy alloys (HEAs) despite presenting the potential to mitigate solid segregation observed in binary and ternary liquid metal systems.^[3,4,7,8] While HEAs are typically characterized in the solid state and present a range of superior mechanical and thermal properties, their unique configurations, with inherently disordered crystal structures and a high concentration of lattice defects, also open a vast, yet relatively unexplored compositional space for a variety of catalytic and reactive applications.^[9–11]

The HEAs are exceptionally promising for catalytic and reactive applications due to the synergistic effects of multielemental constituents, also known as the “cocktail effect”.^[10–13] Most often, the advantageous effects are gained through the elemental dispersion of the added constituents.^[13,14] To date, investigations into solid HEAs for catalysis have focused on defect engineering and strategies for surface and oxide layer doping.^[10,14,15] In contrast to solid systems, we hypothesize that liquid metal solvents offer a dynamic platform for developing multielemental and high-entropy liquid alloy systems. Designing HEAs using metallic solvents has the potential to alleviate challenges related to the miscibility of different elements, resulting in ultra homogeneous dispersion within the liquid matrix, while also probing their activity in the liquid state and maintaining their inherent disorder state. Recently, a method for synthesizing HEA nanoparticles from metal salt precursors and using liquid metal as supports has been reported but ultimately remains in the realm of solid metallurgy.^[16] In contrast, liquid metal solvents provide a dynamic platform for designing multicomponent and high-entropy liquid alloy systems, potentially allowing combination of elements that may be challenging to synthesize by traditional methods, thereby addressing miscibility issues.^[17] In this work, we explored the synthesis of nanoscale high-entropy liquid metal alloys (HELMAs) and examined their morphology, mixed-phase structures composed of atomically dispersed noble metals at elevated concentrations, and assessed their catalytic performance for the hydrogen evolution reaction (HER) at room temperature as a model reaction for benchmarking the functionality of the HELMA nanocatalysts.

2. Results and Discussion

2.1. HELMAs Synthesis

We dissolved an equiatomic mixture of gold (Au), copper (Cu), platinum (Pt), and palladium (Pd) (0.5 at% each) into a gallium (Ga) and indium (In) based eutectic liquid metal solvent (EGaIn) thereby creating multielemental high-entropy liquid metal solutions (**Figure 1a**). Cu and Ga possess nearly identical radii, which facilitates their ability to form substitutional alloys with potentially greater chemical activity. This similarity also holds true for Au and Pt. Entropy calculations of the alloys were conducted in order to predict the behavior of the chosen elements (see theoretical calculations in the Methods). As such, the choice of Cu is further validated by the theoretical calculations that show a

drastic increase in intrinsic entropy of the EGaIn solvent as can be seen in **Figure 1b**. Au, Pt, and Pd were also chosen as model noble catalytic elements in our exploration. Furthermore, the combination of noble metals such as Au, Pt, Pd, along with transition metals like Cu, is common and has been previously investigated for HER.^[18] Pt was specifically selected to examine its elemental dispersibility and HER catalytic activity within these high-entropy configurations. As can be seen in **Figure 1b**, the combination of all these metallic elements provides the highest entropy at room temperature.

Employing a low-impact, two-step synthesis process conducted at near room temperature, the HELMAs were subsequently shaped at the nanoscale utilizing an ultrasonic treatment. The nanoscale liquid metal systems exhibited high-entropy mixes with oxide surfaces enriched in reactive elements, along with the presence of multiple plasmonic states. This simple synthesis strategy led to high-entropy nanomaterials of near-limitless combinations. Initially, the reactive solute elements were thermally dissolved from their respective metallic states into the EGaIn liquid metal base (as illustrated in **Figure 1a**) forming liquid metal melts presenting high configurational entropy (see Methods). The second synthesis step involves generating HELMA nanoparticles via sonication in a thermally controlled dispersion medium to preserve the high-entropy characteristics of the melt and avoid undesired phase segregation within the nanoparticles that can occur during cooling (see Methods). The homogenization effect induced by the sonication of the high-entropy liquid solutions forms nanoscale HELMAs characterized by a combination of a few or all of the Au, Cu, Pt, and Pd elements as schematically represented in **Figure 1c**. As evidenced by the differential scanning calorimetry (DSC) results, shown in **Figure 1d**, the HELMA melts display numerous melting events prior to forming a complete single liquid solution. The initial melting event, common to all the HELMA samples, occurs at around 15 °C and is governed by the liquid metal solvent EGaIn.^[19] This suggests that the primary dissolution of the reactive elements into the metallic media does not fundamentally alter the phase transition behavior of the HELMA solutions at specific concentrations of 0.5 at% each, each exceeding the solubility limit in Ga at room temperature, thereby preserving the core characteristics of the base metallic solvent. Following the initial melting event of the base liquid metal solvent, the subsequent phenomena are associated with the phase transitions of multiple intermetallic compounds and solid solution phases within the high-entropy alloy melts.

The ultrasonic waves generated during sonication effectively disrupt the high surface tension of the HELMAs, consequently forming spherical nanodroplets suspended within the dispersion media.^[20] The sonication procedure consistently yields HELMA nanodroplets with an average diameter approximating 300 nm across all series of samples (**Figure 2a**). This result is consistent with previous studies on liquid metal nanodroplet formation via sonication, which is an established technique known to yield liquid metal droplets with large and controlled size distributions in the micro/nano range.^[20,21] The high-entropy configuration of the six-component (senary) HELMA nanodroplet is illustrated in **Figure 2b**.

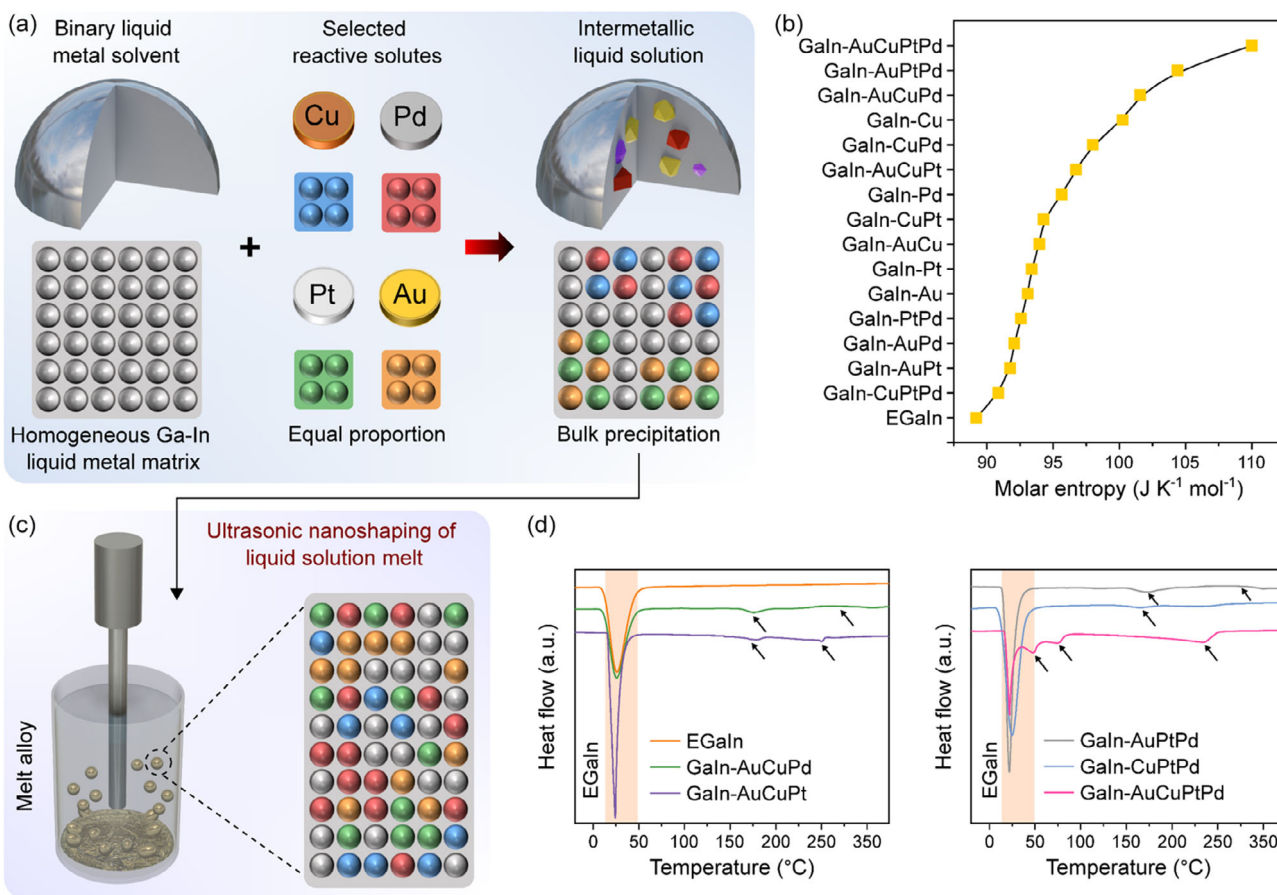


Figure 1. Schematic representation of the synthesis of HELMAs and their thermal analysis. a) Alloying procedure for making HELMAs from equal proportions of reactive elements in a liquid metal matrix and a representation of the possible precipitation reactions of intermetallic compounds in the liquid metallic solution. b) Entropy calculations of selected combination of multicomponent liquid metals and HELMAs. c) Procedure for the fabrication of nanoscale HELMAs via an ultrasonication method and representation of the high-entropy single solution melt. d) Differential scanning calorimetry analysis (DSC) of the HELMAs with arrows highlighting the phase transition events.

2.2. HELMA Nanodroplets Characteristics

Transmission electron microscopy coupled with energy-dispersive X-ray spectroscopy (TEM/EDX) images of EGaIn, as a reference, unveiled a uniform elemental distribution of Ga and In throughout the nanoscale droplets (Figure 2c). A distinct oxide layer of Ga is also discernible on the nanodroplet's surface, which could partially dislodge during the ultrasonic processing. All synthesized HELMA nanoparticles exhibited spherical morphologies resulting from the high surface tension of the liquid metal solvent. The apparent homogeneity highlights the effectiveness of sonication as an accessible tool for realizing balanced elemental dispersion in liquid high-entropy alloy systems at the nanoscale. The corresponding SEM images showing the morphology and size distribution of these nanodroplets are presented in Figure S1, S2, Supporting Information. The structural configuration of the nanodroplets is comprised of a high-entropy metallic core encapsulated within a high-entropy oxide surface layer as presented in Figure 2d and e with additional results in Figure S3, S4, Supporting Information. The high-magnification TEM/EDX image (Figure 2f) shows the apparent

liquid metallic interface of a GaIn-AuCuPtPd nanodroplets. The elemental distribution further demonstrates that the surface Ga oxide layer is enriched with homogeneously distributed Au and Pt and to a lesser extent elemental distribution of Cu and Pd, while the core image represents the homogeneous liquid solution comprised of all elements. The atomic ratio of the HELMA nanodroplets was experimentally determined using inductively coupled plasma optical emission spectroscopy (ICP-OES). All elements were successfully quantified after digestion, further indicating the incorporation of the elements into the HELMA at the nanoscale while presenting minimal deviations from the initial bulk alloy composition (Table S1, Supporting Information). The atomic ratio error for Pt and Pd element was the lowest (8% deviation), while for Au and Cu, the deviations were more significant. The Ga/In ratio deviated by less than 5% for all samples as compared to the initial bulk alloy EGaIn, which provided further confirmation that the composition of the EGaIn liquid metal is retained at the nanoscale.

The electron energy loss spectroscopy (EELS) mapping of an individual HELMA GaIn-AuCuPtPd nanodroplet is presented in Figure 3a, while the EELS mapping of a group of

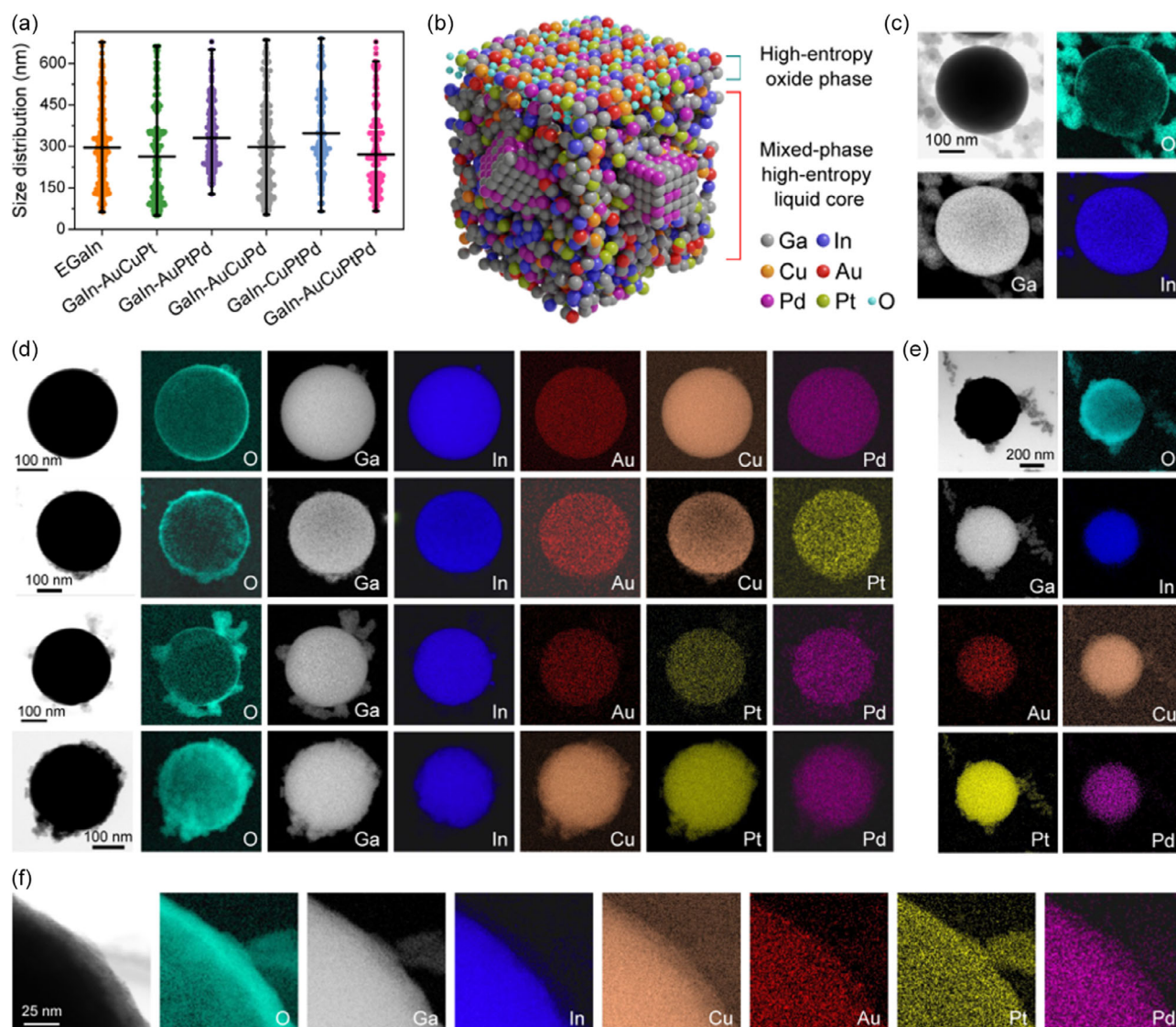


Figure 2. Morphologies of the HELMA nanodroplets. a) Size distributions of the EGaIn and HELMA nanodroplets. b) Schematic representation of the multiphase HELMA nanostructure. c) TEM image and EDX elemental maps of the binary EGaIn metallic solvent at the nanoscale. d) TEM images and EDX elemental maps of the quinary GaIn-AuCuPd, GaIn-AuCuPt, GaIn-AuPtPd and GaIn-CuPtPd HELMA nanodroplets. e) TEM image and EDX elemental maps of the senary GaIn-AuCuPtPd HELMA nanodroplets and f) close-up image and elemental maps of the liquid metallic interface.

GaIn-AuCuPtPd nanodroplets is shown in Figure S5, Supporting Information. The EELS data for EGaIn, for comparison, are found in previous reports.^[8] The EELS spectrum revealed multiple peaks located at 3.6, 6.5, and 12.9 eV (Figure 3b). The EELS mapping corresponding to the identified peaks highlighted the multitiered structure of the HELMA nanodroplet. This intricate configuration was marked by a surface plasmon resonance, an intermediary state, and a bulk plasmon state. Particularly, the peak at 6.5 eV is associated with the surface plasmon resonance characteristic of liquid Ga-In alloys and closely matches previously reported literature.^[8] The peak at 12.9 eV is attributed to the bulk plasmon peak, consistent with previous EELS measurements of EGaIn nanodroplets, however, with a shift to lower intensity, likely due to the presence of the added metallic

elements.^[8] Areas of heightened intensity can also be discerned within the core of the nanodroplets, which correspond to noble metal nanoclusters with increased free electron density compared to that of liquid-phase Ga alloys, further emphasizing the complex mixed liquid–solid microstructure induced by the high entropy. Furthermore, we attributed the peak at 3.6 eV to the presence of a thicker external oxide layer, which is composed of Ga oxide enriched with noble and reactive metallic elements, as evidenced by the correlation between the TEM mapping of the oxide layer (Figure 2f) and the EELS mapping. The near-edge X-ray absorption fine structure in electron yield mode analysis (NEXAFS, see Methods) reveals remarkable similarities in the absorption features of EGaIn and GaIn-AuCuPtPd HELMA, indicating the preservation of the local bonding structure for Ga and

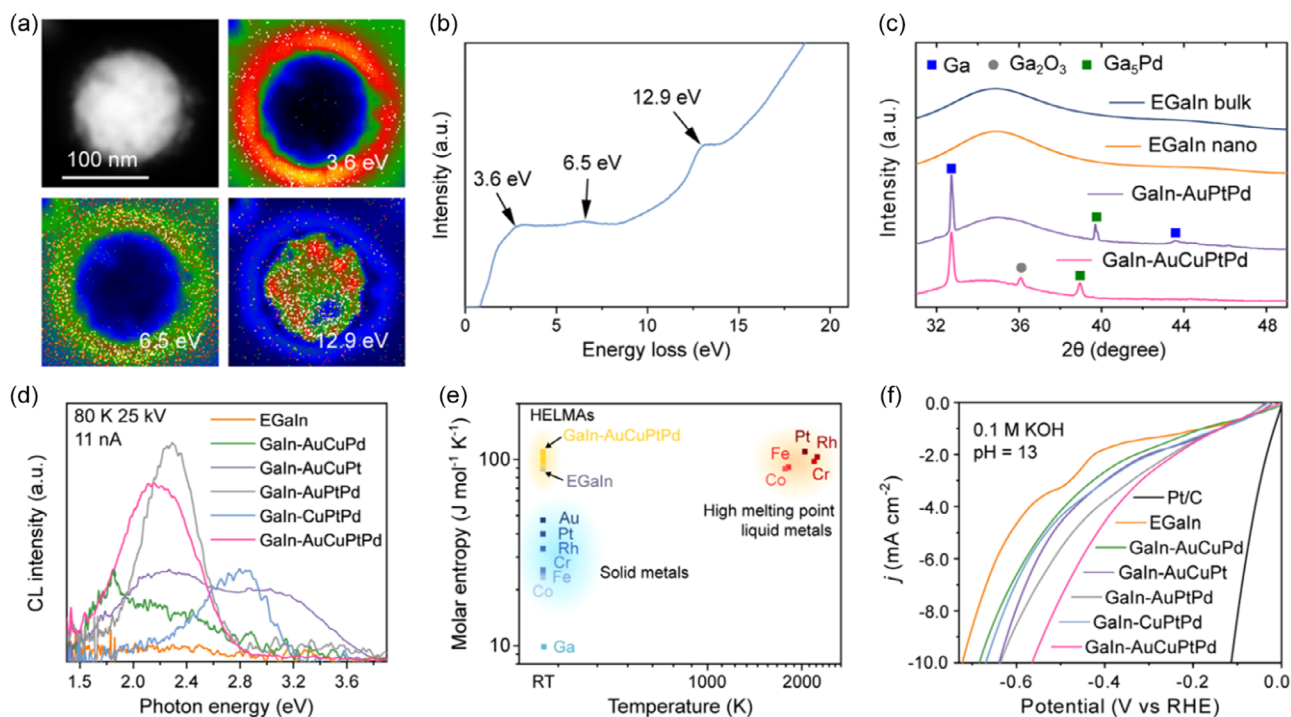


Figure 3. Characterization and HER performance of the HELMA nanodroplets. a) TEM image and EELS maps of a GaIn-AuCuPtPd HELMA nanodroplet and b) associated EELS spectrum with zero-loss peak removal. c) XRD patterns of the EGaIn melt, EGaIn nanodroplets, GaIn-AuPtPd nanodroplets, and senary GaIn-AuCuPtPd HELMA nanodroplets. d) CL spectra of the HELMA nanodroplets. e) Entropy estimates comparison of the HELMA nanodroplets with other reported values for liquid and solid high melting point metals. f) HER activity of the HELMA nanodroplets in 0.1 M KOH alkaline environment.

O in the oxide layer (Figure S6, Supporting Information). Although the Ga absorption edge of the HELMAs is identical to that of the reference β -Ga₂O₃ crystal, indicating a Ga³⁺ oxidation state, the spectral features diverge significantly due to the noncrystalline nature of the HELMA oxide layer. The wider *L*₃ peaks observed in the HELMA suggest a reduction in Ga-O coordination. Both the EGaIn and HELMA O K-edge spectra exhibit a pre-edge absorption peak at ≈ 0.5 eV below the conduction band minimum. This feature indicates the formation of a subband within the bandgap of Ga₂O₃, attributable to O-In bonds. Importantly, the NEXAFS spectra of Pt and Pd at the M_{4,5} edge, depicted in Figure S6, Supporting Information, show identifiable absorption peaks, confirming the incorporation of these elements within the oxide layer of the GaIn-AuCuPtPd HELMA nanodroplets. These observations highlight the complex and diverse electronic structures of the HELMA nanodroplets and also reveal their potential applications in optoelectronics and catalysis. The feature from the EELS measurements, determined at 1.9 eV, was associated with the oxide skin of GaIn-AuCuPtPd and was validated through the Tauc plot obtained from ultraviolet-visible (UV-vis) absorption spectroscopy analysis (Figure S7, Supporting Information). This contrasts with the oxide layer of EGaIn, which is typically reported to be around 3.6 eV.^[22] The values exhibit a decreasing trend as the number of constituents within the alloy increased demonstrating the effect of compositional complexity on the high-entropy oxide layer covering the HELMA nanodroplets.

To comprehensively investigate the liquid state, atomic dispersion of added elements characterize the nanosized domains within the HELMA nanodroplets, X-ray diffraction (XRD) assessments were performed. For comparative reference, the XRD patterns of both the bulk EGaIn melt and nanodroplets are shown in Figure 3c and present the characteristic patterns associated with liquid state Ga. The XRD patterns of the GaIn-AuPtPd and GaIn-AuCuPtPd nanodroplets (also shown in Figure 3c) and of the other HELMA nanodroplets (Figure S8, Supporting Information) revealed distinct mixed multiphase states, evidenced by the presence of peaks that can be assigned to Ga-based intermetallic and oxide species. Remarkably, no peak indicative of the presence of intermetallic Pt with Ga or Pt itself could be observed in the GaIn-AuCuPtPd and GaIn-AuPtPd patterns. The Ga₅Pd intermetallic phase was consistently identified across all samples that contain Pd.^[6,23] In certain samples, the presence of the Ga₂Pt phase was also detected, suggesting that segregation of Pt can occur, depending on the elemental composition and entropy configuration of the HELMAs.^[3] To further elucidate the nanoscale segregation phenomena in the HELMA nanodroplets, we performed single-particle cathodoluminescence (CL) spectroscopy at an accelerating voltage of 25 kV which excited the entire nanoparticles. Fluorescent nanoclusters of noble metals, especially those of Pt, have been extensively reported, and the potential formation of such nanoclusters in the HELMA nanoparticles was investigated using CL.^[24] The CL spectrum of the HELMA nanodroplets of

GaIn-AuCuPt, shown in Figure 3d, exhibited two emission bands at 2.2 and 3.0 eV regions, which are attributed to nanoclusters of Au and Pt with less than 20 atoms of the noble metals.^[25] Interestingly, Au nanoclusters were present in all samples containing Au, while the presence of Pt nanoclusters varied depending on the specific alloy composition. The CL spectra, acquired under identical excitation conditions, demonstrated that the concentration of Au nanoclusters in the HELMA nanodroplets decreases with the addition of Cu to the equiatomic mixture possibly due to the Cu effect of enhancing the entropy of the system, as also predicted by the entropy calculations. This suggests a competitive interplay between the lattice energies of the noble metals and solvation effects. Notably, the non-detection Pt nanocluster luminescence in both GaIn-AuPtPd and GaIn-AuCuPdPt HELMA nanostructures confirms the dispersion of Pt atoms at a discrete scale within the liquid metal matrix, rather than their assembly into distinct nanoclusters.

We correlated the nanoscale structures of the HELMAs with their high-entropy characteristics. The entropy of HELMAs, sensitive to the relative weight differences of the constituent elements, enables access to high-entropy characteristics, similar to those observed in molten Pt at 2045 K.^[26] Within the HELMA materials, these high-entropy characteristics are attainable at both room temperature and nanoscale dimensions comparably to high-melting point molten metals (Figure 3e). In these high-entropy regimes, Pt remains uniformly dispersed within the matrix of the liquid metal nanodroplet matrix without the formation of nanoclusters, unlike what is observed in lower entropy systems where Pt nanoclustering was observed, as evidenced by the XRD and CL analyses. This highlights the unique material behaviors inherent to high-entropy liquid metal configurations.

Leveraging the combinatory architecture of the HELMA nanodroplets composed of active constituents, we envision substantial potential in catalytic applications.^[27] As a representative example, we utilized HER to illustrate the tunability of this system with subsequent inclusion of metallic elements. At present, one of the challenges of HER is to reach the atomically dispersed Pt realm within catalysts. When evaluated for HER, we observed that the selected elements incorporated into the HELMA nanodroplets have beneficial properties as electrocatalysts as compared to the low reactivity EGaIn liquid metal matrix. HER performances were assessed in alkaline media (0.1 M KOH), which was chosen for its compatibility with Ga-based liquid metal systems containing dilute catalytic elements and to mitigate unwanted reactions that can be prevalent in more extreme conditions.^[4] In alkaline media (Figure 3f), the GaIn-AuCuPtPd electrode, which includes all active elements and presents the highest entropy, displayed the highest activity with the lowest HER overpotential (−570 mV vs RHE at 10 mA cm^{−2}, Figure 3f). Figure S9, Supporting Information, presents the cyclic voltammetry curves in 0.1 M KOH of the GaIn-AuCuPtPd HELMA nanodroplets and the subsequent stability test of the catalyst for HER activity following 3000 cycles. The HELMA nanodroplets demonstrate high stability, and only a slight increase in overpotential was observed to achieve a current density of 10 mA cm^{−2} for HER after cycling. For comparison, Pt/C catalysts are known to exhibit low stability in alkaline media.^[28]

The morphology and surface characteristics of the GaIn-AuCuPtPd nanodroplets were evaluated after HER and following 3000 cycles. The HELMA nanodroplets showed no significant morphological changes, as seen in the SEM images in Figure S10, Supporting Information. Furthermore, we analyzed the surface elemental composition of the GaIn-AuCuPtPd nanodroplets before and after electrolysis and cycling using X-ray photoelectron spectroscopy (XPS, Figure S11, Supporting Information). The Ga 2*p* spectra of the HELMA nanodroplets before reaction showed two deconvoluted peaks corresponding to Ga(III) (Ga₂O₃, 1117.03 eV) and a faint peak centered at 1115.13 eV corresponding to metallic Ga. After reaction, the peak associated with metallic Ga was not observed, which could indicate greater surface oxidation of the nanodroplets. The analysis of the In 3*d* spectra shows the presence of unchanged peaks centered at 444.47 eV associated with In(III) oxide species (In₂O₃) before and after HER. Similarly, the Au 4*f* and Pt 4*f* spectra showed persistent peaks before and after reaction. The shift to higher binding energies for the peak associated with Pt 4*f* (71.72 eV) was attributed to the local environment of the Pt atoms being surrounded by Ga atoms.^[4] The Au 4*f* spectra exhibited a characteristic peak centered at 84.56 eV, corresponding to Au, with a shift to higher energy previously reported for supported catalysts containing Au.^[29] Finally, the Cu 2*p* spectra presented very weak peaks centered at 932.68 eV observable before and after reaction that may indicate the Cu(I) oxidation state of copper within the Ga oxide layer.^[30] However, Pd was not detected on the XPS spectrum, which was attributed to its tendency to form intermetallic clusters within the liquid particle cores as shown in the XRD analysis (Figure 3c). The minimal morphological and surface composition changes confirmed the stability of the GaIn-AuCuPtPd nanodroplets under these conditions.

Remarkably, the entropy characteristics of the HELMA nanodroplets correlate with catalytic performance, especially under high-entropy conditions. In these high-entropy regimes, Pt is atomically dispersed within the liquid metal matrix, thus avoiding the formation of nanoclusters, unlike in low-entropy systems where Pt clustering is typically observed. This was also demonstrated by the GaIn-AuPtPd sample, which exhibited the second-highest level of entropy and a lack of Pt clusters, as confirmed by CL analysis (Figure 3d). Interestingly, the reduction of the Ga oxide layer, which was observed in the linear sweep voltammetry (LSV) curve of EGaIn nanodroplets, was not evident with the HELMA nanodroplets possibly due to the doping phenomena of the oxide layers as observed in the TEM/EDX images (Figure 2f). While commercial Pt/C catalysts are commonly regarded as the standard for HER activity, other factors, in addition to the presence of Pt, contribute to the HER performance of the HELMAs nanodroplets. Nevertheless, the significant impact of Pt is highlighted by the comparatively lower performance of the base EGaIn liquid metal and GaIn-AuCuPd systems. For comparison, the LSV curves of the HELMA nanodroplets were normalized based on the calculated surface area of the catalysts and Pt loading content (see Methods).

3. Conclusion

In conclusion, we presented an approach for the design and synthesis of nanoscale high-entropy liquid metal state alloys,

encompassing noble metals in mild conditions and environments. The calculated entropy of the room temperature HELMAs exceeds those of solid HEAs and also of very high-temperature molten metals and alloys, establishing a route to create high-entropy liquid metal systems under ambient conditions. The novel HELMA nanodroplets feature a high-entropy liquid solution core of atomically dispersed metallic elements, with nanosized domains of other noble metals, and high-entropy surface oxide shells. The high-entropy characteristics of the HELMA nanodroplets effectively limit multiphase segregation of solid and intermetallic species at high elemental concentrations. Furthermore, we uncovered competing solvation phenomena within the nanoscale liquid metal matrix of the HELMA nanodroplets, which could be leveraged for selective atomic dispersion of metallic elements. We showed that the atomic dispersion of Pt in the ternary GaIn-AuCuPtPd nanocatalysts led to an enhancement in catalytic activity in comparison to less entropic combinations. Our work presents the first step into the vast and nearly limitless compositional space of HELMAs and leads to considerable scope for further enhancement and fine-tuning of this emerging class of catalysts. Beyond noble metals, liquid metal solvents open the possibility to incorporate a wide range of elements, including earth-abundant elements and more exotic materials, such as reactive rare earth, providing opportunities for the customization of purpose-built high-entropy liquid metal-based systems utilizing the full spectrum of the periodic table.

4. Experimental Section

Sample Preparation: Gallium and indium beads (99.999% purity, Indium Corporation) were first alloyed at the eutectic ratio in a glass tube on a hotplate at 350 °C for 3 h to form the binary EGaIn metallic solvent. The reactive elements were added at an equal concentration of 0.5 at% in the liquid metal solvent. To form the high-entropy liquid metals, gold, copper, palladium, and platinum in the form of wires (purity \geq 99.99%, sourced from Sigma-Aldrich) were dissolved into the EGaIn phase on a hotplate at 550 °C for 5 h. The nanoparticles were prepared by ultrasonication of the liquid melts in a relatively high boiling point liquid phase (glycerol). The high-temperature sonication process was performed using a probe sonicator (VCX 750, Sonics & Materials, Inc.) at 22% power for 30 min. The temperature was kept constant at 250 °C using a hotplate. The obtained nanoparticles were then washed with ethanol using centrifugation before characterization.

Sample Characterizations: SEM/EDX (JEOL InTouchScope, JSM-IT500HR, paired with a JEOL, Ex-74600U4L2Q model, EDX detector) was employed to characterize the morphology and elemental distribution across the samples. The morphologies and elemental distribution of the samples were further analyzed using HRTEM (JEM-F200, JEOL) coupled with an EDX detector system. The samples did not require coating prior to imaging due to their high electrical conductivities. The size distributions of the nanoparticles were determined through analysis of SEM images, utilizing ImageJ software. A Netzsch DSC 204 F1 instrument was utilized for the DSC measurements.

The proportion of each element in the HELMA nanodroplets was determined using ICP-OES (PerkinElmer, USA). The samples were first digested in a mixture of HNO₃ and HCl (1:3 vol/vol) before analysis.

EELS mapping and spectroscopy were performed using JEOL JEM-F200 TEM equipped with Gatan GIF Continuum-S spectrometer and cold FEG operating at 200 kV. The EELS measurements were performed in scanning-TEM (STEM) mode. The mapping was obtained with a resolution of 2 nm/pixel with 20 accumulations and exposure of 1 ms/pixel. The lowest channel dispersion of 0.015 eV/Ch was selected, and the zero-peak

loss (ZLP) auto detection and lock and object tracking were enabled during mapping acquisition. The emission current was lowered to 5 μ A during the EELS measurements to enhance the ZLP-FWHM to 0.4 eV. The ZLP was removed using the standard reflected tail method, and individual peaks in the low-loss region were fitted using the Lorentzian–Drude model. The model fit and maps were generated using Gatan Micrograph 3.4 software.

UV-vis spectroscopy was carried out using a Cary 5000 UV-vis-NIR spectrophotometer (Agilent Technologies) for the determination of the bandgaps of the nanoscale samples. The crystal structures of the melts and nanoscale samples were characterized using the X'pert Multipurpose X-ray diffraction (MPD) system ($\lambda = 1.5418$ Å, Cu-K α radiation). Cathodoluminescence (CL) spectroscopy was conducted using an FEI Quanta SEM fitted with a parabolic mirror light collector, a QE65000 spectrometer, and a cryostat stage regulated by liquid nitrogen (N₂) temperature controller. All CL spectra underwent correction to account for the total system response.

The investigation of the local electronic structure around Ga, O, Pd, and Pt atoms in the base EGaIn alloy and in the GaIn-AuCuPtPd HELMA alloy was conducted using NEXAFS on the Soft X-Ray Spectroscopy beamline of the Australian Synchrotron. The X-ray absorption process was quantified using a channeltron detector, which captured the emitted electrons resulting from the X-ray absorption. X-ray photoelectron spectroscopy was performed on an ESCALAB250Xi spectrometer (Thermo Scientific, UK) with a monochromatic incident radiation was Al K α X-rays.

Electrochemical Characterization: Electrochemical measurements were carried out with a CHI760D workstation (CH Instruments Inc., USA) integrated with a rotating ring disk electrode apparatus (PINE Research, USA) in a typical H-cell system separated by an anion-exchange membrane (A201, Tokuyama, Japan). A glassy carbon electrode (GCE, 5 mm in diameter) loaded with different catalysts was used as the working electrode. A graphite rod was used as the counter-electrode throughout the measurements, and an Ag/AgCl (in saturated KCl) electrode was used as the reference electrode.^[51] All HELMA samples were deposited on the freshly cleaned and polished GCE. Commercially available Pt/C catalyst was also deposited on a GCE for comparison (10 wt% Pt loading, Fuel Cell Store, USA). All working electrodes were prepared by dispersing 0.1 mg of catalyst powder in 1:1 solution of ethanol and deionized water (vol/vol), followed by the addition of 30 μ L of Nafion solution (Sigma-Aldrich, 99.99%). The resulting mixture was ultrasonicated for 30 min to form a homogeneous ink, a volume of 8 μ L was then deposited on the GCEs.

Linear sweep voltammetry (LSV) curves were determined in N₂-saturated 0.1 M KOH electrolyte (giving an electrolyte pH of 13), at 5.0 mV s⁻¹ from 0.1 to -0.6 V (vs. RHE). All polarization curves were automatically corrected for the iR contribution from the cell. The working electrode was rotated at a speed of 1600 rpm to alleviate the accumulation of evolved hydrogen bubbles on the GCE surface. The recorded potential was converted to a reversible hydrogen electrode (RHE) according to the Nernst equation: $E_{\text{RHE}} = E_{\text{Ag/AgCl}} + 0.059 \times \text{pH} + 0.197$. The electrochemical measurements were performed in a controlled laboratory environment of 21 °C average room temperature.

The performance of the HELMA electrodes was normalized to that of the commercial Pt/C catalyst based on their respective reported and calculated surface areas and taking into account the Pt loading, which is 10 wt% for the Pt/C catalyst and averages \approx 1.2 wt% for the HELMAs. The accessible surface area of Pt in the 10 wt% Pt/C catalyst is reported to be 120 m² g⁻¹ (provided by the manufacturer), with Pt present in the form of crystallites ranging from 2 to 3 nm in diameter. For comparison, the HELMA nanodroplets have an average diameter of 300 nm. The difference in Pt loading content and surface areas represents a scaling factor of 50 times, accordingly, for comparative analysis between the Pt/C and HELMA electrodes. However, this value does not include the liquid properties of the HELMA nanoparticles or the impact of soft-sphere stacking, which, if considered, might suggest an even higher scaling factor to evaluate the performance of the electrodes.

Theoretical Calculation of Entropy: The hard-sphere model is a useful tool for calculating various thermodynamic properties of liquid metals and their alloys. In this study, we employed this model to calculate the

entropy of liquid metals. We assumed that the density of the mixture remains unaffected at room temperature and that the number of microstates remains constant for all alloys, disregarding any influence from structural factors

$$S = S_0 - R \left[\frac{4n - 3n^2}{(1 - n)^2} - 2n \right] \quad (1)$$

where S_0 is the entropy of an ideal gas considering the parameters of a liquid metal

$$S_0 = \frac{5}{2}R + \frac{3}{2}R \ln \left[\frac{mkT\nu^{\frac{2}{3}}}{2\pi h^2 N^{\frac{2}{3}}} \right] \quad (2)$$

where R is the gas constant, m is the mass of a single microstructure; k is the Boltzmann constant, $\nu = \frac{\mu}{\rho}$ (where μ is molar weight of microstructure and ρ is the density at a room temperature), h is the Planck constant, N is the Avogadro number, and n is the density of atom packing. The second term in (1) is configuration entropy.

Supporting Information

Supporting Information is available from the Wiley Online Library or from the author.

Acknowledgements

The authors thank the Surface Analysis Laboratory at the Mark Wainwright Analytical Centre, UNSW. This work has been accomplished with the support of the Australian Research Council (ARC), ARC Discovery Projects (DP230102813 and DP240101086) and ARC Laureate Fellowship grant (FL180100053). This research was partially undertaken on the soft X-ray spectroscopy beamline at the Australian Synchrotron, part of ANSTO.

Conflict of Interest

The authors declare no conflict of interest.

Author Contributions

F.M.A. and K.K.Z.: Conceptualization; F.M.A., M.B.G., A.Z., R.D. and R.A.: data curation; F.M.A., S.N., M.B.G., A.Z., Z.P., R.D., M.B., C.A.E., M.M., C.T.T. and K.J.L.: methodology; F.M.A., M.B.G., A.Z., J.L., L.B., Y.C., S.R., A.K.S., C.P.I., M.S.W., R.D. and T.D.: investigation; F.M.A., R.D., A.Z., Z.P., M.A.R., R.A., J.T., S.R., D.E., A.R.J., C.T.T., N.H. and T.D.: formal analysis; F.M.A., R.A. and K.K.Z.: funding acquisition; K.K.Z.: supervision, F.M.A.: writing—original draft; F.M.A., R.A. and K.K.Z.: writing, review and editing.

Data Availability Statement

The data that support the findings of this study are available from the corresponding author upon reasonable request.

Keywords

high-entropy alloy, high-entropy liquid metal alloy, liquid metal

Received: June 12, 2024
Published online: June 30, 2024

- [1] a) T. Daeneke, K. Khoshmanesh, N. Mahmood, I. A. de Castro, D. Esrafilzadeh, S. J. Barrow, M. D. Dickey, K. Kalantar-Zadeh, *Chem. Soc. Rev.* **2018**, *47*, 4073; b) M. D. Dickey, *ACS Appl. Mater. Interfaces* **2014**, *6*, 18369; c) S.-Y. Tang, C. Tabor, K. Kalantar-Zadeh, M. D. Dickey, *Annu. Rev. Mater. Res.* **2021**, *51*, 381.
- [2] a) F.-M. Allieux, M. B. Ghasemian, W. Xie, A. P. O'Mullane, T. Daeneke, M. D. Dickey, K. Kalantar-Zadeh, *Nanoscale Horiz.* **2022**, *7*, 141; b) A. Zavabeti, J. Z. Ou, B. J. Carey, N. Syed, R. Orrell-Trigg, E. L. H. Mayes, C. Xu, O. Kavehei, A. P. O'Mullane, R. B. Kaner, K. Kalantar-Zadeh, T. Daeneke, *Science* **2017**, *358*, 332; c) R. Yuan, Y. Cao, X. Zhu, X. Shan, B. Wang, H. Wang, S. Chen, J. Liu, *Adv. Mater.* **2024**, *36*, 2309182; d) J.-Y. Gao, S. Chen, T.-Y. Liu, J. Ye, J. Liu, *Mater. Today* **2021**, *49*, 201; e) X. Li, L. Cao, B. Xiao, F. Li, J. Yang, J. Hu, T. Cole, Y. Zhang, M. Zhang, J. Zheng, S. Zhang, W. Li, L. Sun, X. Chen, S.-Y. Tang, *Adv. Sci.* **2022**, *9*, 2105289; f) Q. Shen, M. Jiang, R. Wang, K. Song, M. H. Vong, W. Jung, F. Krisnadi, R. Kan, F. Zheng, B. Fu, P. Tao, C. Song, G. Weng, B. Peng, J. Wang, W. Shang, M. D. Dickey, T. Deng, *Science* **2023**, *379*, 488; g) J. Ma, F. Krisnadi, M. H. Vong, M. Kong, O. M. Awartani, M. D. Dickey, *Adv. Mater.* **2023**, *35*, 2205196.
- [3] S. A. Idrus-Saidi, J. Tang, S. Lambie, J. Han, M. Mayyas, M. B. Ghasemian, F.-M. Allieux, S. Cai, P. Koshy, P. Mostaghimi, K. G. Steenbergen, A. S. Barnard, T. Daeneke, N. Gaston, K. Kalantar-Zadeh, *Science* **2022**, *378*, 1118.
- [4] M. A. Rahim, J. Tang, A. J. Christofferson, P. V. Kumar, N. Meftahi, F. Centurion, Z. Cao, J. Tang, M. Baharfar, M. Mayyas, F.-M. Allieux, P. Koshy, T. Daeneke, C. F. McConville, R. B. Kaner, S. P. Russo, K. Kalantar-Zadeh, *Nat. Chem.* **2022**, *14*, 935.
- [5] a) D. Esrafilzadeh, A. Zavabeti, R. Jalili, P. Atkin, J. Choi, B. J. Carey, R. Brkljača, A. P. O'Mullane, M. D. Dickey, D. L. Officer, D. R. MacFarlane, T. Daeneke, K. Kalantar-Zadeh, *Nat. Commun.* **2019**, *10*, 865; b) T. Bauer, S. Maisel, D. Blaumeiser, J. Vecchiotti, N. Taccardi, P. Wasserscheid, A. Bonivardi, A. Görling, J. Libuda, *ACS Catal.* **2019**, *9*, 2842; c) D. Wang, J. Ye, Y. Bai, F. Yang, J. Zhang, W. Rao, J. Liu, *Adv. Mater.* **2023**, *35*, 2303533; d) H. Lu, S.-Y. Tang, J. Zhu, X. Huang, H. Forgham, X. Li, A. Shen, G. Yun, J. Hu, S. Zhang, T. P. Davis, W. Li, R. Qiao, *Adv. Funct. Mater.* **2024**, *34*, 2311300.
- [6] N. Taccardi, M. Grabau, J. Debuschewitz, M. Distaso, M. Brandl, R. Hock, F. Maier, C. Papp, J. Erhard, C. Neiss, W. Peukert, A. Görling, H. P. Steinrück, P. Wasserscheid, *Nat. Chem.* **2017**, *9*, 862.
- [7] a) F.-M. Allieux, S. Merhebi, M. B. Ghasemian, J. Tang, A. Merenda, R. Abbasi, M. Mayyas, T. Daeneke, A. P. O'Mullane, R. Daiyan, R. Amal, K. Kalantar-Zadeh, *Nano Lett.* **2020**, *20*, 4403; b) F.-M. Allieux, S. Merhebi, J. Tang, S. A. Idrus-Saidi, R. Abbasi, M. G. Saborio, M. B. Ghasemian, J. Han, R. Namivandi-Zangeneh, A. P. O'Mullane, P. Koshy, R. Daiyan, R. Amal, C. Boyer, K. Kalantar-Zadeh, *Adv. Funct. Mater.* **2020**, *30*, 1907879; c) J. Tang, R. Daiyan, M. B. Ghasemian, S. A. Idrus-Saidi, A. Zavabeti, T. Daeneke, J. Yang, P. Koshy, S. Cheong, R. D. Tilley, R. B. Kaner, R. Amal, K. Kalantar-Zadeh, *Nat. Commun.* **2019**, *10*, 4645; d) S. A. Idrus-Saidi, J. Tang, M. B. Ghasemian, J. Yang, J. Han, N. Syed, T. Daeneke, R. Abbasi, P. Koshy, A. P. O'Mullane, K. Kalantar-Zadeh, *J. Mater. Chem. A* **2019**, *7*, 17876.
- [8] S.-Y. Tang, D. R. G. Mitchell, Q. Zhao, D. Yuan, G. Yun, Y. Zhang, R. Qiao, Y. Lin, M. D. Dickey, W. Li, *Matter* **2019**, *1*, 192.
- [9] a) Y. Xin, S. Li, Y. Qian, W. Zhu, H. Yuan, P. Jiang, R. Guo, L. Wang, *ACS Catal.* **2020**, *10*, 11280; b) H. Li, J. Lai, Z. Li, L. Wang, *Adv. Funct. Mater.* **2021**, *31*, 2106715.
- [10] D. B. Miracle, O. N. Senkov, *Acta Mater.* **2017**, *122*, 448.
- [11] G. Feng, F. Ning, J. Song, H. Shang, K. Zhang, Z. Ding, P. Gao, W. Chu, D. Xia, *J. Am. Chem. Soc.* **2021**, *143*, 17117.

- [12] a) M. W. Glasscott, A. D. Pendergast, S. Goines, A. R. Bishop, A. T. Hoang, C. Renault, J. E. Dick, *Nat. Commun.* **2019**, *10*, 2650; b) D. Zhang, H. Zhao, X. Wu, Y. Deng, Z. Wang, Y. Han, H. Li, Y. Shi, X. Chen, S. Li, J. Lai, B. Huang, L. Wang, *Adv. Funct. Mater.* **2021**, *31*, 2006939.
- [13] S. Nellaiappan, N. K. Katiyar, R. Kumar, A. Parui, K. D. Malviya, K. G. Pradeep, A. K. Singh, S. Sharma, C. S. Tiwary, K. Biswas, *ACS Catal.* **2020**, *10*, 3658.
- [14] G. M. Tomboc, T. Kwon, J. Joo, K. Lee, *J. Mater. Chem. A* **2020**, *8*, 14844.
- [15] a) H. Li, Y. Han, H. Zhao, W. Qi, D. Zhang, Y. Yu, W. Cai, S. Li, J. Lai, B. Huang, L. Wang, *Nat. Commun.* **2020**, *11*, 5437; b) M. Cui, C. Yang, S. Hwang, M. Yang, S. Overa, Q. Dong, Y. Yao, A. H. Brozena, D. A. Cullen, M. Chi, T. F. Blum, D. Morris, Z. Finfrock, X. Wang, P. Zhang, V. G. Goncharov, X. Guo, J. Luo, Y. Mo, F. Jiao, L. Hu, *Sci. Adv.* **2022**, *8*, eabm4322.
- [16] G. Cao, J. Liang, Z. Guo, K. Yang, G. Wang, H. Wang, X. Wan, Z. Li, Y. Bai, Y. Zhang, J. Liu, Y. Feng, Z. Zheng, C. Lu, G. He, Z. Xiong, Z. Liu, S. Chen, Y. Guo, M. Zeng, J. Lin, L. Fu, *Nature* **2023**, *619*, 73.
- [17] a) J. Tang, A. J. Christofferson, J. Sun, Q. Zhai, P. V. Kumar, J. A. Yuwono, M. Tajik, N. Meftahi, J. Tang, L. Dai, G. Mao, S. P. Russo, R. B. Kaner, M. A. Rahim, K. Kalantar-Zadeh, *Nat. Nanotechnol.* **2024**, *19*, 306; b) Y. Yu, G. Liu, S. Jiang, R. Zhang, H. Deng, E. A. Stach, S. Bao, Z. Zeng, Y. Kang, *Nano Res.* **2023**, *16*, 10742; c) L. Huang, P.-C. Chen, M. Liu, X. Fu, P. Gordiichuk, Y. Yu, C. Wolverton, Y. Kang, C. A. Mirkin, *Proc. Natl. Acad. Sci.* **2018**, *115*, 3764.
- [18] X. Huang, G. Yang, S. Li, H. Wang, Y. Cao, F. Peng, H. Yu, *J. Energy Chem.* **2022**, *68*, 721.
- [19] a) J. Tang, X. Zhao, J. Li, R. Guo, Y. Zhou, J. Liu, *ACS Appl. Mater. Interfaces* **2017**, *9*, 35977; b) M. D. Dickey, R. C. Chiechi, R. J. Larsen, E. A. Weiss, D. A. Weitz, G. M. Whitesides, *Adv. Funct. Mater.* **2008**, *18*, 1097.
- [20] Y. Lin, J. Genzer, M. D. Dickey, *Adv. Sci.* **2020**, *7*, 2000192.
- [21] S.-Y. Tang, R. Qiao, Y. Lin, Y. Li, Q. Zhao, D. Yuan, G. Yun, J. Guo, M. D. Dickey, T. J. Huang, T. P. Davis, K. Kalantar-Zadeh, W. Li, *Adv. Mater. Technol.* **2019**, *4*, 1800420.
- [22] M. B. Ghasemian, M. Mayyas, S. A. Idrus-Saidi, M. A. Jamal, J. Yang, S. S. Mofarah, E. Adabifiroozjaei, J. Tang, N. Syed, A. P. O'Mullane, T. Daeneke, K. Kalantar-Zadeh, *Adv. Funct. Mater.* **2019**, *29*, 1901649.
- [23] a) N. Iwasa, T. Mayanagi, N. Ogawa, K. Sakata, N. Takezawa, *Catal. Lett.* **1998**, *54*, 119; b) Z. Rzyńska, P. Wiśniewski, D. Kaczorowski, W. Xie, R. J. Cava, T. Klimczuk, M. J. Winiarski, *J. Phys. Chem. C* **2021**, *125*, 11294.
- [24] S.-I. Tanaka, J. Miyazaki, D. K. Tiwari, T. Jin, Y. Inouye, *Angew. Chem., Int. Ed.* **2011**, *50*, 431.
- [25] a) J. Zheng, C. Zhou, M. Yu, J. Liu, *Nanoscale* **2012**, *4*, 4073; b) X. Wang, L. Zhao, X. Li, Y. Liu, Y. Wang, Q. Yao, J. Xie, Q. Xue, Z. Yan, X. Yuan, W. Xing, *Nat. Commun.* **2022**, *13*, 1596; c) J. Bornacelli, H. G. Silva-Pereyra, L. Rodríguez-Fernández, M. Avalos-Borja, A. Oliver, *J. Lumin.* **2016**, *179*, 8.
- [26] a) M. C. Gao, M. Widom, *J. Phys. Chem. B* **2018**, *122*, 3550; b) P. Singh, K. N. Khanna, *Pramana* **1984**, *23*, 511; c) N. E. Dubinin, A. A. Yuryev, N. A. Vatolin, *Thermochim. Acta* **2011**, *518*, 9; d) B. N. Tewari, B. S. Bhargava, K. N. Khanna, *Phys. Status Solidi B* **1982**, *114*, K31; e) V. V. Tekuchev, D. P. Kalinkin, I. V. Ivanova, *Russ. J. Phys. Chem. A* **2018**, *92*, 819.
- [27] D. Wu, K. Kusada, Y. Nanba, M. Koyama, T. Yamamoto, T. Toriyama, S. Matsumura, O. Seo, I. Gueye, J. Kim, L. S. Rosantha Kumara, O. Sakata, S. Kawaguchi, Y. Kubota, H. Kitagawa, *J. Am. Chem. Soc.* **2022**, *144*, 3365.
- [28] a) A. Zadick, L. Dubau, N. Sergent, G. Berthomé, M. Chatenet, *ACS Catal.* **2015**, *5*, 4819; b) Y. Jia, Y. Li, Q. Zhang, S. Yasin, X. Zheng, K. Ma, Z. Hua, J. Shi, C. Gu, Y. Dou, S. Dou, *Carbon Energy* **2024**, 2024, e528.
- [29] J. Radnik, C. Mohr, P. Claus, *Phys. Chem. Chem. Phys.* **2003**, *5*, 172.
- [30] H. Li, R. Abbasi, Y. Wang, F. M. Allieux, P. Koshy, S. A. Idrus-Saidi, M. A. Rahim, J. Yang, M. Mousavi, J. Tang, M. B. Ghasemian, R. Jalili, K. Kalantar-Zadeh, M. Mayyas, *J. Mater. Chem. C* **2020**, *8*, 1656.
- [31] a) J. N. Hansen, H. Prats, K. K. Toudahl, N. Mørch Secher, K. Chan, J. Kibsgaard, I. Chorkendorff, *ACS Energy Lett.* **2021**, *6*, 1175; b) G. Jerkiewicz, *ACS Catal.* **2022**, *12*, 2661; c) M. A. Bird, S. E. Goodwin, D. A. Walsh, *ACS Appl. Mater. Interfaces* **2020**, *12*, 20500.